



# Obstacle-free planar hybrid micromixer with low pressure drop

Sajad Razavi Bazaz<sup>1,2</sup> · Hoseyn A. Amiri<sup>3,4,5</sup> · Steven Vasilescu<sup>1</sup> · Ali Abouei Mehrizi<sup>6</sup> · Dayong Jin<sup>2,7</sup> · Morteza Miansari<sup>3,5</sup> · Majid Ebrahimi Warkiani<sup>1,2,7,8</sup>

Received: 8 April 2020 / Accepted: 3 July 2020  
© Springer-Verlag GmbH Germany, part of Springer Nature 2020

## Abstract

Planar micromixers with repetitive units have received substantial research interest since they allow low cost, lab-on-a-chip (LOC), and point-of-care (POC) systems to achieve a proper level of mixing for any given process. This paper presents an efficient planar micromixer that combines four types of mixing units, including convergent–divergent, circular, rhombic, and G-shaped micromixers. Their combinations and resulting effects on the mixing efficiency are numerically and experimentally investigated. A comprehensive Taguchi design of experiment method was used to reduce the number of the combinations from 1024 to only 16, among which a micromixer made of rhombic and G-shaped units readily showed a mixing efficiency beyond 80% over a wide range of inlet Reynolds numbers 0.001–0.3 and 35–65; meanwhile, a pressure drop as low as 12 kPa was reported. The velocity and concentration fields and their gradients within the nominated micromixer were analyzed, providing a better understanding of the mixing mechanism. These results offer design insights for further development of planar micromixers with repetitive unites for low-cost LOC and POC devices.

**Keywords** Planar mixing units · Optimization · Numerical simulation · Chaotic advection · Mixing index · Pressure drop

Sajad Razavi Bazaz and Hoseyn A. Amiri contributed equally as the first authors.

**Electronic supplementary material** The online version of this article (<https://doi.org/10.1007/s10404-020-02367-x>) contains supplementary material, which is available to authorized users.

- ✉ Ali Abouei Mehrizi  
abouei@ut.ac.ir
- ✉ Morteza Miansari  
mmiansari@nit.ac.ir
- ✉ Majid Ebrahimi Warkiani  
majid.warkiani@uts.edu.au

- <sup>1</sup> School of Biomedical Engineering, University of Technology Sydney, Sydney, NSW 2007, Australia
- <sup>2</sup> Institute for Biomedical Materials and Devices (IBMD), Faculty of Science, University of Technology Sydney, Sydney, NSW 2007, Australia
- <sup>3</sup> Micro+Nanosystems and Applied Biophysics Laboratory, Department of Mechanical Engineering, Babol Noshirvani University of Technology, P.O. Box 484, Babol, Iran

## 1 Introduction

Microfluidic devices continue to have a considerable impact on various fields, including chemical synthesis, biomedical diagnostics, and drug development (Tavassoli et al. 2018; Lashkaripour et al. 2018a; Yi et al. 2006). Microfluidic systems are able to achieve levels of control unapproachable in lab-scale operations, such as highly repeatable conditions, geometric control, well-behaved

- <sup>4</sup> Sensors and Integrated Bio-MEMS/Microfluidics Laboratory, School of Mechanical Engineering, Iran University of Science and Technology, Tehran, Iran
- <sup>5</sup> Department of Cancer Medicine, Cell Science Research Center, Royan Institute for Stem Cell Biology and Technology, ACECR, Isar 11, Babol 47138-18983, Iran
- <sup>6</sup> Department of Life Sciences Engineering, Faculty of New Sciences and Technologies, University of Tehran, Tehran, Iran
- <sup>7</sup> SUSTech-UTS Joint Research Centre for Biomedical Materials and Devices, Southern University of Science and Technology, Shenzhen 518055, People's Republic of China
- <sup>8</sup> Institute of Molecular Medicine, Sechenov University, Moscow 119991, Russia

mixing conditions, environmental control, and small consumption of reagents (Whitesides 2006; Kwon et al. 2017). The flow channels within microfluidic systems possess large surface to volume ratios, owing to their diminutive scale (Condina et al. 2019; Razavi Bazaz et al. 2020a; Raoufi et al. 2020). As a result, an elevated level of energy and mass transfer can be exploited for ever-increasing lab-on-a-chip (LOC) and point-of-care (POC) applications that require mixing. Micromixers provide an elegant platform to quickly reach a desirable level of mixing for a given process. For instance, droplet-based micromixer systems have been used for single-cell screening, proteomic, and genomic analysis (Brouzes et al. 2009; Lashkaripour et al. 2018b). Chemical analysis also benefits from the application of microfluidics; Wang et al. reported the use of an integrated microfluidic chip for the quantification of methanol (Wang et al. 2012), while Fu et al. reported the use of integrated microfluidics for the analysis of formaldehyde in Chinese herbs (Fu et al. 2014). Moreover, various forms of nanoparticles (NPs) have reportedly been synthesized in microfluidics devices, including gold NPs (AuNP) and nanorods (Uson et al. 2016), titanium dioxide NPs (Eun et al. 2009), palladium NPs and copper NPs (Boken et al. 2016). Many of these applications require the rapid and efficient mixing of samples and reagents, which is facilitated by micromixers (Mahmoodi et al. 2019; Mahmoudi et al. 2019), as was showcased by antibody/particle conjugations (Vasilescu et al. 2020).

Micromixers can be integrated with other microfluidic devices to form a lab-on-a-chip system, where they play a vital role in improving the mixing efficiency of a laminar flow regime (Hessel et al. 2005). These micromixers can be categorized as either active or passive (Nguyen and Wu 2004). Active micromixers rely upon the application of external forces to facilitate mixing, where these forces can be thermal, magnetic, acoustic, or electro-kinetic. Although active micromixers provide high levels of mixing efficiency, their structural complexity, difficult integration into microfluidic systems, and cost make them less viable options. Passive micromixers, on the other hand, require no external energy input, other than the application of chaotic advection or turbulence through variation in channel geometry and consequently fluid hydrodynamics (pressure and velocity) (Cai et al. 2017; Bahiraei et al. 2018). These micromixers are more cost-effective and are easily fabricated for integration with other microfluidic components when compared to active ones as they require no complicated-external input source (Lee et al. 2016; Bahiraei et al. 2017). They are an ideal choice for applications that do not require intensive environmental control with less structural complexity. In passive micromixers, mixing is a result of either diffusion

or chaotic advection generated by pumping energy and channel geometry (Bahiraei and Mazaheri 2018a).

The geometry of passive micromixers has been the subject of many reviews over recent years (Bayareh and Ashani 2019; Gambhire et al. 2016; Lee and Fu 2018). Efficient micromixer designs and orientations are crucial to achieving a high mixing index; as such, many designs catering to many different applications have been reported (Bayareh and Ashani 2019). There exist designs containing repetitive and non-repetitive units. Those with a non-repetitive design pattern are manipulated to create either Dean vortices or chaotic advection, increasing the mixing index (Lee et al. 2016; Bahiraei and Mazaheri 2018b; Rasouli et al. 2018). Those with two or more units repeated along the length of the microchannel can be further categorized into three groups, i.e., planar mixing units with repetitive units (without obstacles) (MURU), planar mixing units with repetitive obstacles (MURO), and mixing units with repetitive 3D units (MUR3DU) (Bazaz et al. 2018). MUR3DU micromixers are not easily integrated with other components in lab-on-a-chip devices and are more challenging to fabricate than their planar counterparts. Moreover, MURO micromixers have embedded obstacles within their structure, leading to an increase in the pressure drop along the channel length and are not a suitable candidate for specific microfluidic applications, uniquely portable microfluidic devices.

There exist manifold research studies requiring low-pressure input as well as high mixing efficiency for their applications. Most of the static or dynamic single-cell trappings' devices work with extremely low-flow rates (in the order of  $\mu\text{l/h}$ ) (Nilsson et al. 2009). Also, the separation of nanoparticles (e.g., extracellular vesicles, exosomes, proteins, and DNA ligands) requires flow operation at an extremely low input flow rate (Zhang et al. 2020). For instance, Liu et al. proposed a microchannel based on viscoelastic flows allowing their systems to accommodate velocities up to  $200 \mu\text{l/h}$  (Liu et al. 2017). These studies highlight the need for micromixers working at low pressure while possessing high mixing efficiency. Therefore, micromixers with MURU have gained more publicity in these areas (Chung and Shih 2007). Although numerous planar mixing units without obstacles have been developed for low-pressure input and portable microfluidic devices, further research and optimizing the combination of these units are absent in the literature. The selection of the right sequence of micromixers becomes critical as the mixing efficiencies within each class of micromixers vary substantially. That is, each individual mixing unit, even if repeated, may not meet the requirements of every application.

The primary aim of this study is to propose a micromixer configuration that maintains a low-pressure drop while

creating the highest mixing efficiency possible. To achieve this, we created a hybrid micromixer comprised of a combination of planar mixing units. To this end, various MURUs have been analyzed, and the best combination has been selected via the Taguchi optimization method. To integrate different and inconsistent units, we have used Reynolds (Re) and Péclet numbers (Pe) to keep dynamic and geometric similarities constant. Afterwards, the optimal design has been investigated thoroughly, i.e., the effect of Re on the performance of the whole mixer, the mixing performance of each unit, and the mixing mechanism behind the best one. Finally, the pressure drop within the selected micromixer is calculated and compared with the previously developed MURO micromixer (Bazaz et al. 2018). Through this optimization method, we have developed a planar hybrid micromixer with low-pressure input suitable for the resource-limited facilities and low-flow rate fluid applications such as single-cell analysis or antibody-particle conjugations.

## 2 Materials and methods

In this section, the governing equations and the design of experiment method (DOEM) used to select the best combinations are explained along with the selected MURU. The theoretical and geometric considerations for the design are also outlined, followed by the device manufacturing process.

### 2.1 Governing equations and boundary conditions

The numerical method was executed using the physics described in Table 1. The Re range for this study lies within the laminar flow region. We consider the properties of the fluid to be similar to those of water, as such, we are able to apply the incompressible isothermal steady-state Navier–Stokes equation (Eq. 1a) coupled with the continuity equation (Eq. 1b). These two equations are solved for  $2V$  and  $P$  as variables, where they are the velocity vector field and the fluid pressure, respectively. Concentration distribution,  $c$ , is calculated by solving the stationary convective–diffusive

transport equation (Eq. 2) with  $2V$  being passed from the previously solved equations (segregated scenario) and  $D$  being the diffusivity between the fluids.

In the laminar flow equation,  $\rho$  and  $\mu$  are the density and dynamic viscosity of the fluid, respectively. A uniform velocity ( $U$ ) boundary condition was assigned to the flow inlets, and the atmospheric pressure was set to the outlet to emulate the experimental condition. Other boundaries were regarded as no-slip walls, and their validity checked by confirming the Knudsen number (Eq. 3) held a value below  $10^{-3}$ :

$$\text{Kn} = \frac{\lambda}{L_c}, \quad (3)$$

wherein  $\lambda$  denotes the mean free path length (0.25 nm for water) and  $L_c$  represents the characteristic length of the channel. As a result, a Kn of approximately  $1.7 \times 10^{-6}$  was obtained, which means that the no-slip condition at the walls and the principle of the continuum are reasonable assumptions. Finally, the uniform molar concentration of 0 and 1 was set at the inlets as the boundary conditions for the transport of diluted species equation. Furthermore, the final molar intensity of 0.5 infers that the fluids are adequately mixed.

The abovementioned equations were discretized and solved by COMSOL Multiphysics 5.2a, a commercial finite element analysis (FEA) software (Mollajan et al. 2018). The segregated scenario has been utilized, having the velocity and pressure solved first (with quadratically discretized concentration calculated at the previous step), followed by the concentration (with the linearly discretized velocity and pressure achieved during this step). Each equation is solved by the iterative solver, restarted Generalized Minimum RESidual scheme (GMRES), proved efficient for sparse linear systems. All simulations have been conducted with a 64-bit operating system, Intel Xeon E312 (Sandy Bridge) processor, and 31.0 GB of memory. The result of mesh independency analysis using Richardson extrapolation is provided in Table S1 and Fig. S1 in the Electronic Supplementary Information (ESI) along with the quality of the grid.

**Table 1** Constitutive equations, simulation parameters, and boundary conditions (BC) assigned to each boundary per physics

Physics	Equation		Physical properties	Boundary	BC
Laminar flow	$\rho(2V \cdot \nabla)2V = -\nabla P + \mu \nabla^2 2V$ $\nabla \cdot 2V = 0$	(1a)	$\rho = 988 \text{ kg/m}^3$	Inlet 1	$2V = U$
		(1b)	$\mu = 8.9 \times 10^{-4} \text{ Pa} \cdot \text{s}$	Inlet 2	$2V = U$
				Outlet	$P = 0$
				Walls	$2V = 0$
Transport of diluted species	$(2V \cdot \nabla)c = D \nabla^2 c$	(2)	$D = 2 \times 10^{-9} \text{ m}^2/\text{s}$	Inlet 1	$c = 1 \text{ mol/m}^3$
				Inlet 2	$c = 0 \text{ mol/m}^3$
				Outlet	$\frac{\partial c}{\partial 2n} = 0$
				Walls	$\frac{\partial c}{\partial 2n} = 0$

## 2.2 Design of experiment method and MURU selection

To design an appropriate micromixer, a DOE was employed to efficiently select and test combinations of planar mixing units without obstacles. As shown in Fig. 1, four MURUs including, convergent–divergent wall (Afzal and Kim 2012, 2015; Ansari et al. 2010), Circular (Ansari et al. 2010), Rhombic (Hossain and Kim 2014), and G-shaped mixing units (Bhopte et al. 2010) were selected. Having unique characteristics, each unit affects the flow differently to maximize the generation of chaotic advection. The first chosen unit was a convergent–divergent wall design made up of sinusoidal channel walls. The main channel is split and recombined at a

regular interval. This design reportedly generates differential centrifugal forces and a double vortex pair at the necks of the channel (Afzal and Kim 2012). The circular MURU design features an unbalanced split and recombination of the main channel about a circular center. The two created sub-channels are of different widths, collectively adding to the width of the main channel. The greater sub-channel possesses a larger mass flow rate, resulting in a higher level of inertia. The difference in inertia between the two sub-channels creates an unbalanced collision of fluids as the channels recombine, increasing the level of turbulence (Li et al. 2013). The selected rhombic MURU follows a similar design strategy in that it also utilizes an unbalanced split and recombine (SAR) system. The selected design follows a three-split system between a rhombic angle of

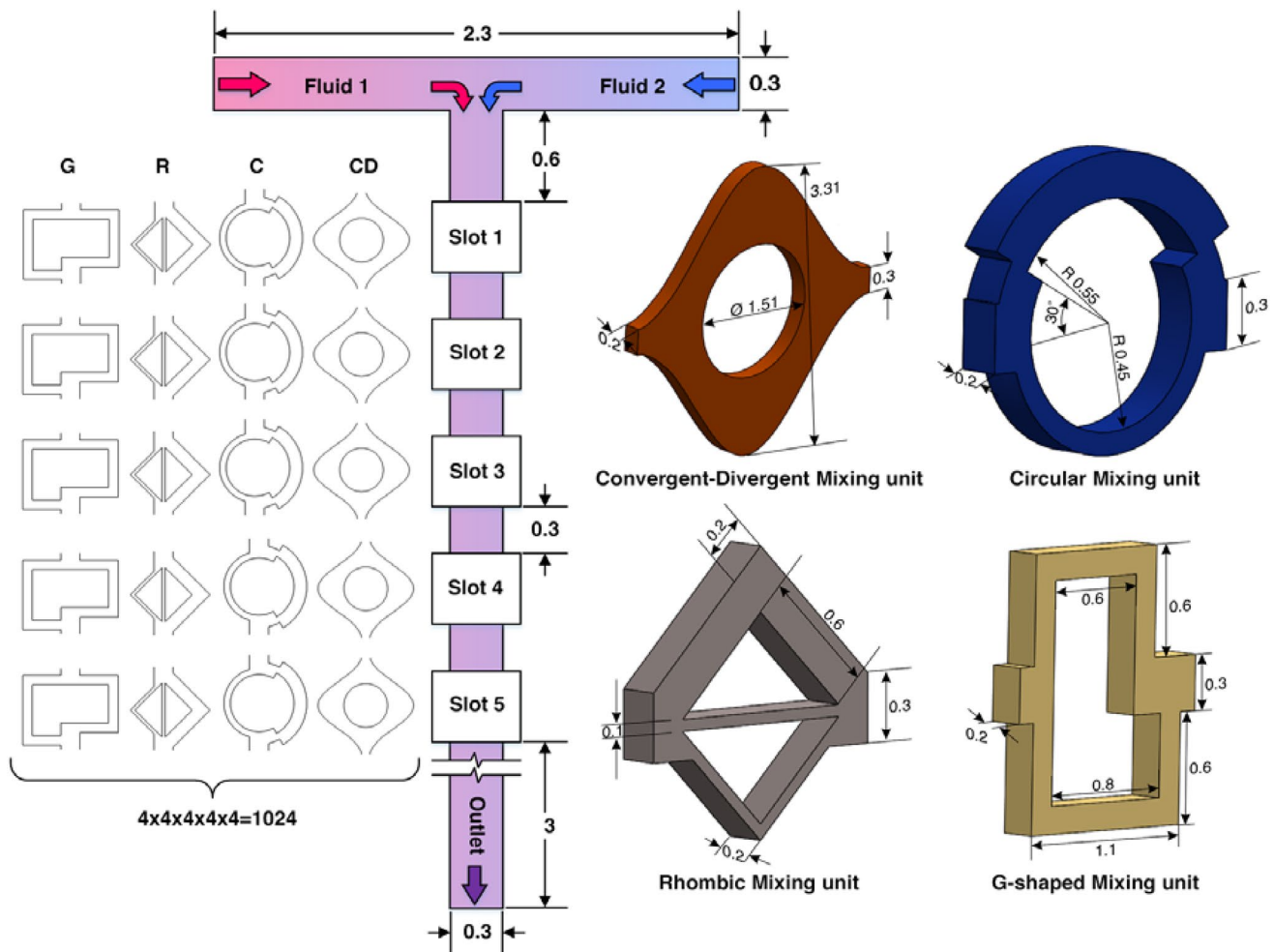


**Fig. 1** The schematic view of the hybrid micromixer consisting of 5 equally distant slots for sequentially locating the selected units (all dimensions are in mm). The directions of convergent–divergent and G-shaped units are parallel to the main flow, while the main flow in the rhombic and circular units, pouring through the wider branch, determines the unit direction (all the directions in the scheme are

downward). CD, C, R, and G stand for each level, namely convergent–divergent, circular, rhombic, and G-shaped mixing units, respectively. All of the possible placements of each unit (1024), which will be reduced to 16 using the Taguchi elimination method to find an efficient configuration

45°. The three-split system generates extra recirculation flows, enhancing the mixing index. This type of rhombic MURU typically exhibits superior mixing capabilities compared to a two-split system in the recombination zone when placed in series. Hossain and Kim reported the use of this three-split system in series where the major and minor sub-channels are inverted along the length of the micromixer (Hossain and Kim 2014). The final unit is a G-shaped unit proposed by Bhoppte et al. (2010). Here, the fluids travel in a square wave pattern after being split. Sharp changes in the fluid flow direction facilitate shear mixing to improve the mixing efficiency. The recombination of channels then merges the fluids into a lateral stream once more. In our study, all mixing units have a constant 200 µm height.

The present micromixer provides five slots for mixing units, as shown in Fig. 1. However, fitting all of these units into five slots yields 1024 ( $4^5$ ) possible combinations, impractical to simulate and fabricate within the timeframe of this study. To address this, a Taguchi  $L_{16}$  ( $4^5$ ) orthogonal array optimization was used to reduce the total number of experimental designs to 16. This method itself was developed by Genichi Taguchi and has been widely used for experimental design optimization (Lashkaripour et al. 2019). Here, we have four design parameters (the selected mixing units) with five levels of value for each (number of slots). This yields an  $L_{16}$  orthogonal array with the specific combinations and orders of mixing units, as tabulated in Table 2.

Equation (4) was used to determine the minimum number of experiments:

$$N = 1 + N_V(L - 1), \quad (4)$$

where  $N$  is the minimum number of experiments,  $N_V$  is the total number of variables, and  $L$  is the number of levels of each variable. Using this equation, where  $N_V = 4$  and  $L = 5$ , leads to an  $N$  value of 16 experiments.

### 2.3 Scaling of mixing units and dynamic similarity

It is essential to mention that the units chosen are of similar scales in terms of volume and overall dimensions. This helps to ensure their compatibility in both simulative and physical experiments while maintaining their optimum state, in this case, geometrical parameters. Each unit was scaled about its centroid based on the dimensional relationships and aspect ratios reported in the literature and described in our previous study (Bazaz et al. 2018).

To ensure each unit was scaled correctly and performed under the same conditions, both  $Re$  and  $Pe$  were set equal during the scaling process.  $Re$  is the determinant of a fluid flow characteristic and defined as the ratio of inertia to viscous forces as presented in Eq. (5):

$$Re = \frac{\rho U D_h}{\mu}, \quad (5)$$

where  $D_h = 4A/P$  is the hydraulic diameter of channel wherein  $A$  is the area of the channel's cross-section, and  $P$  is its wetted perimeter (Razavi Bazaz et al. 2020b). In this study,  $Re$  of each inlet was calculated and reported.  $Pe$  number, given in Eq. (6), represents the ratio of the convective to the diffusive mass transfer, indicating that the mixing process is more predominant by either factor.

$$Pe = \frac{UD_h}{D}. \quad (6)$$

### 2.4 Quantification of mixing

The mixing index (MI) is one of the primary forms of determining the efficiency of mixing used in this study. The MI is defined by Eq. (7) as follows:

$$MI = 1 - \sqrt{\frac{1}{n} \sum_{i=1}^n \left( \frac{k_i - \bar{k}}{\bar{k}} \right)^2}, \quad (7)$$

where  $n$  is the number of sample points,  $k_i$  is the molar fraction at the cross-section of the outlet, and  $\bar{k}$  is 0.5 as the average molar fraction. An MI value of 1 is indicative of complete mixing while an MI value of 0 indicates no mixing.

**Table 2** The combination of mixing units for optimization test scenarios proposed by Taguchi for five factors and four levels

Experiment no.	Slot 1	Slot 2	Slot 3	Slot 4	Slot 5
1	CD	CD	CD	CD	CD
2	CD	C	C	C	C
3	CD	R	R	R	R
4	CD	G	G	G	G
5	C	CD	C	R	G
6	C	C	CD	G	R
7	C	R	G	CD	C
8	C	G	R	C	CD
9	R	CD	R	G	C
10	R	C	G	R	CD
11	R	R	CD	C	G
12	R	G	C	CD	R
13	G	CD	G	C	R
14	G	C	R	CD	G
15	G	R	C	G	CD
16	G	G	CD	R	C

## 2.5 Fabrication process

Micromixers were fabricated from a mold made by photolithography. Briefly, the mixture of polydimethylsiloxane (PDMS) pre-polymer and curing agent (Sylgard 184, DowSilCorp., Midland, MI, USA) were first mixed (ratio of 10:1) and then degassed in a vacuum chamber. This mixture was then poured on a silanized mold, followed by baking in an oven at 70 °C for 2 h. Thereafter, the cured PDMS was gently peeled off from the mold, and inlets and the outlet were punched using a Uni-Core™ Puncher (Sigma-17 Aldrich Co. LLC, SG). Finally, the PDMS channel was bonded onto a glass slide using an oxygen plasma machine (Harrick Plasma, USA) (Fig. S2). Once the channel was fabricated, samples were introduced into the chip using a syringe pump (Harvard Co., USA) and images and videos were captured via a CCD camera (DP80, Olympus, Tokyo, Japan) mounted on an inverted microscope (IX73, Olympus, Tokyo, Japan).

To ensure the fabricated chips retained the desired dimensions, their cross-sections were measured via profilometry (Fig. S3). Profilometry data was then used to calculate the hydraulic diameter from the cross-sections of design numbers 5 (Fig. S3A) and 9 (Fig. S3B). Since micromixers are velocity-sensitive cases, the hydraulic diameter calculation is vital for syringe pump flow rates to improve accuracy.

## 3 Results and discussion

### 3.1 Numerical validation

To reduce the cost and time, the optimization process was carried out using the numerical results from the specific configurations suggested by the Taguchi optimization method. All of the simulations are performed for a Re of 5, a regular value for lab-on-chip microdevices. To validate the numerical results, we randomly selected a number of designs for fabrication and conducting the experiments. Figure 2a–c compares the numerical and experimental results of design numbers 5, 9, and 13, respectively. To extract the experimental values of the mixing index, an image processing software (Fiji) has been used. Using this software, grayscale values of the images along a line parallel to the channel width at the inlet and outlet have been extracted. These values were then normalized using Eq. (8):

$$I_i = \frac{I_i^* - I_{\min}^*}{I_{\max}^* - I_{\min}^*}, \quad (8)$$

where the actual intensity is represented by  $I_i^*$ , and the minimum and maximum values of intensity at the inlet (unmixed fluid) are given by  $I_{\min}^*$  and  $I_{\max}^*$ , respectively. The

experimental value of the mixing index is then calculated using Eq. (9):

$$MI_{\text{experimental}} = 1 - \frac{ME}{ME_{\text{no mixing}}}. \quad (9)$$

Here, ME and  $ME_{\text{no mixing}}$  were calculated using Eqs. (10) and (11).

$$ME = \sqrt{\frac{1}{N} \sum_{i=1}^N \left( \frac{I_i - \bar{I}}{\bar{I}} \right)^2} \quad (10)$$

$$ME_{\text{no mixing}} = \sqrt{\frac{1}{N} \sum_{i=1}^N \left( \frac{I_{\min, \max} - \bar{I}}{\bar{I}} \right)^2}, \quad (11)$$

where  $N$  is the number of pixel in the inlet or outlet image along a line parallel to the channel width,  $\bar{I}$  is 0.5, and  $I_{\min, \max}$  can be 0 or 1, respectively. The extracted values of the experimental mixing index are illustrated in Fig. 2. Both quantitative and qualitative results illustrate that the numerical predictions agree well with the experimental results of the selected designs, further proving the reliability of the results produced by the computational fluid dynamics (CFD) method in micromixers.

### 3.2 Taguchi optimization results

Figure 3 presents the results of the Taguchi optimization (Table 2) based on the mixing index of each channel. These results provide the sensitivity of each factor and their placement along the channel. Scattered graphs are colored based on the order of the numerical tests (runs) following the Taguchi table (Fig. 3a–e). The performance of each unit was evaluated at least once per slot. In other words, simulations were fairly carried out using all optimization factors and their levels to capture those effects. The highest mixing indexes across each slot were obtained in numerical test numbers 10 and 15, respectively shown as cyan and orange, as highlighted with green circles. Comparing the unit combinations in these two cases shows that both of them have the CD unit located at slot 5, meaning that the CD unit is not a good candidate for slot 5, and the contributions of other units are more effective. Moreover, the use of CD and C units in each slot appears to be inefficient, as marked with red circles shown by blue colors scatter (Fig. 3a–e).

Signal to noise ratio (S/N), a parameter derived from the Taguchi method, was used to analyze the performance of each unit. Three classes of quality can be utilized, each assigned to a category that states the-lower-the-better,

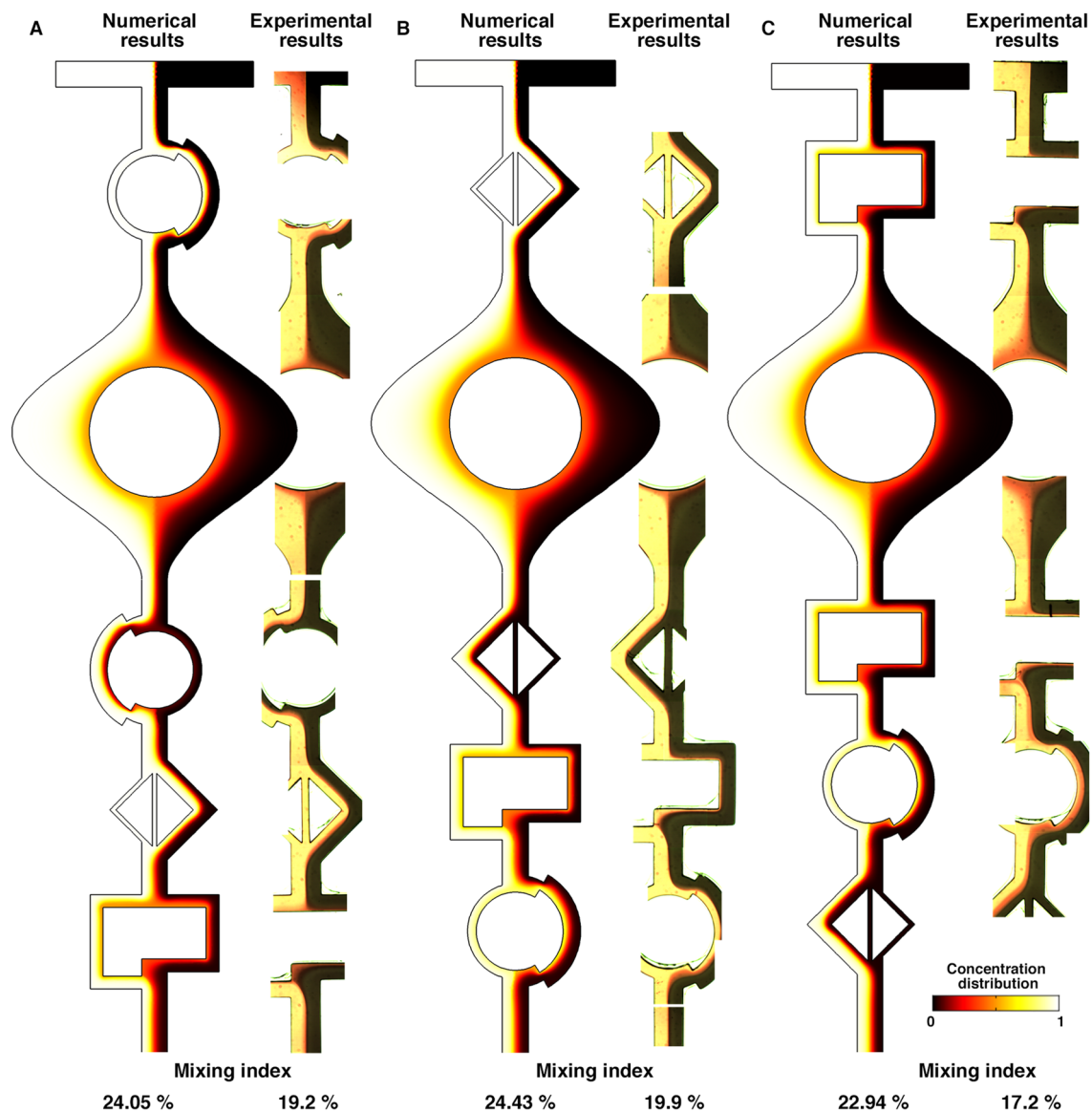


**Fig. 2** Comparisons of numerical and experimental results at the left and the right of each column, respectively, on the distribution of concentration in **a** design 5, **b** design 9, and **c** design 13 (Table 2). Upon comparison, a reliable correlation is observed between the experi-

mental and simulation results; that is, the numerical results can accurately and efficiently envisage the flow behavior that occurs in real scenarios

the-nominal-the-better, and the-higher-the-better. To maximize the mixing efficiency, we have selected the-higher-the-better criterion, since the mixing index was the optimization goal. After selecting the proper class, the signal to noise ratio (S/N) quantifies the degree of response to the target response under various noise conditions. The formula corresponding to this feature is written as Eq. (12):

$$S/N = -10 \times \log_{10} \left( \frac{1}{n} \sum_{i=1}^n \left( \frac{1}{Y^2} \right) \right), \quad (12)$$

where  $n$  is the number of responses in the factor level combination, and  $Y$  is the responses for the given factor level combination (mixing index here). By looking at the S/N diagram for each slot at  $Re = 5$ , the best-nominated units for each slot are specified by the same color arrow pointing the highest value (Fig. 3f). The Taguchi method suggests that the optimum configuration is constituted of three R units where two of them are placed at slot 1 and 2, and the third one is located in slot 4 between two G units. As a result, this verifies our previous predictions about CD and C units' inefficiency and accordingly highlighting the high mixing

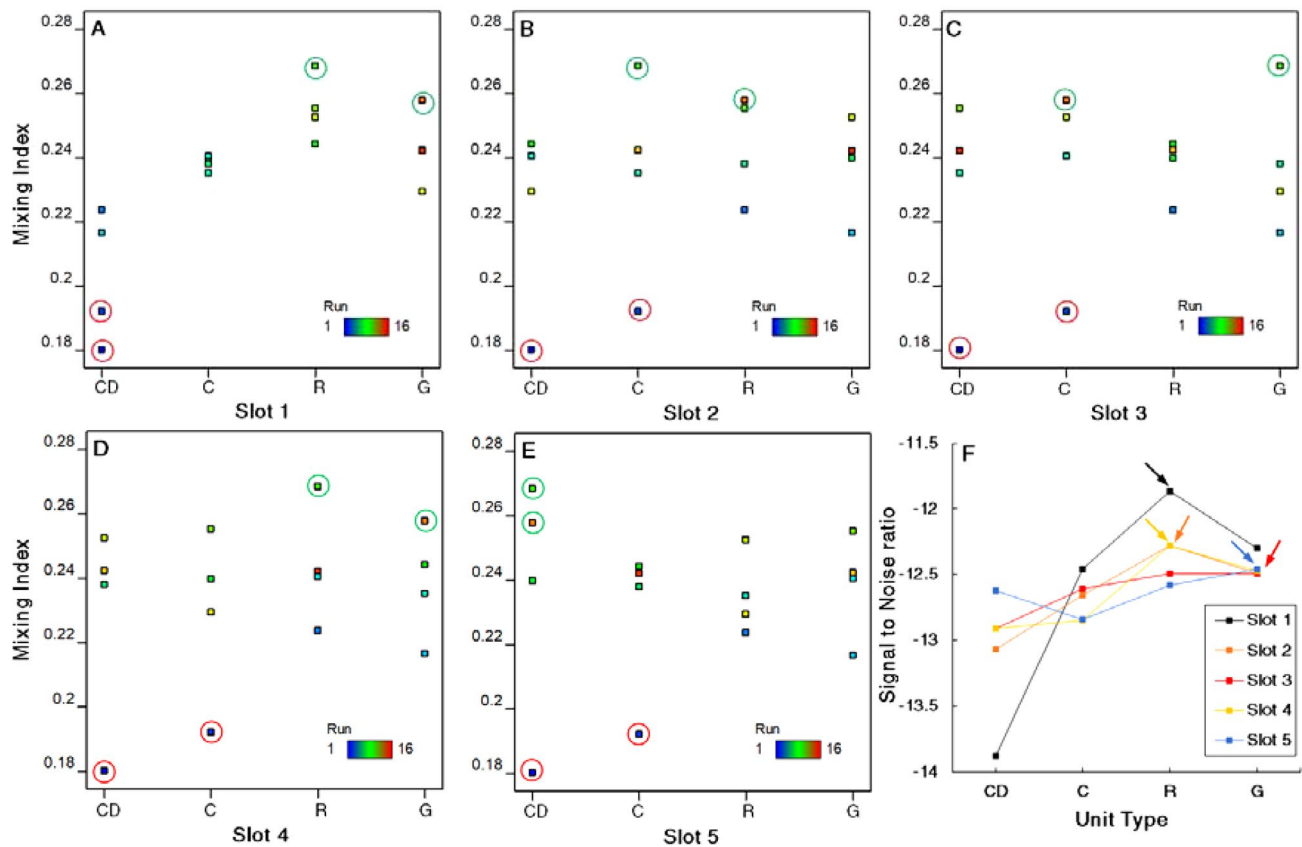


**Fig. 3** a–e Performance and sensitivity of each unit placed in each slot along with **f** their signal to noise ratio. Green circles indicate the highest mixing indexes due to the placement of a specific unit, while

the red circles are for the lowest indexes. Arrows indicate the nominated units in the slots of a similar color (color figure online)

efficiency of R and G units. Furthermore, the first slot is shown to be more sensitive to the change of the inserted mixing units compared to other slots (Fig. 3).

Figure 4 depicts the mixing mechanism of the optimum hybrid MURU micromixer at two Re of 0.5 and 60. These two low and high Re were selected to separately study the effect of each mixing mechanism, i.e., diffusive and convective, depending on the critical inlets Re. Diffusion is dominant in Re below its critical value, while the effect of convection is insignificant to some extent and vice versa. The gradient of concentration at different sections is demonstrated along with a comparison between the diffusive and convective flux magnitude for a better understanding of their underlying mechanisms. The homogeneity of concentration gradient throughout the channel means there is no sign of convection mixing, and this can be confirmed by the arrows of convective flux. The convective flux is larger by an order of magnitude in some regions, but the key factor is its nonhomogeneity to break the fluid laminae and blend them. On the other hand, the mixing mechanism of the optimum design at low Re is mostly based on the diffusion where the approximately uniform convective flux does

not play a significant role. Thus, the mixing index gradually increases after each section. However, fluid characteristics and consequently, the concentration gradient distribution changes drastically at high Re, where the convection mixing mechanism is dominant. This is proved by the extreme diversity of the concentration gradient pattern in each section. A straightforward interpretation is shown by the direction of convective flux (Fig. 4). Fluid starts to be unstable after passing the first unit owing to its inertia and the transverse/in-plane velocity components. As a result of employing SAR units, double and quadruple counter-rotating vortices form, respectively after each R unit (Sects. 2, 3 and, 5) and after each G unit (Sects. 4 and 6). As the convective flux changes, the fluid interface changes accordingly to assist the mixing performance. This phenomenon, called chaotic convection, reduces the diffusion path. The most efficient unit featuring this mechanism is the G unit located in the third slot, contributing more than 30% to the performance of the hybrid micromixer.

Figure 5 depicts the mixing index trend versus the horizontal length of the channel. It takes into account the effect of each unit at different Re. Figure 5a demonstrates the

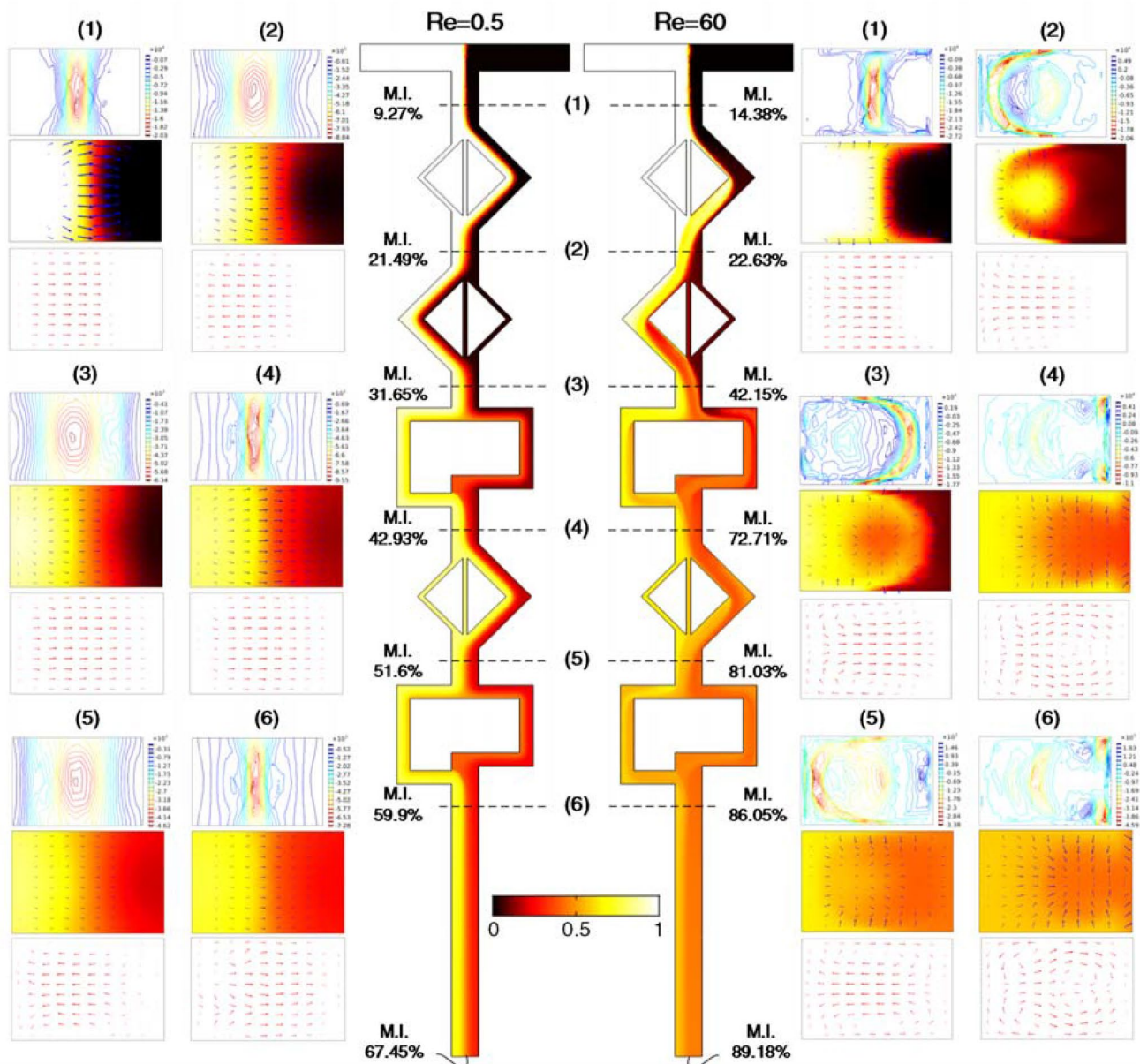


**Fig. 4** Analysis of mixing mechanism at different sections along the length of micromixer for the two different Re of 0.5 and 60. Sectional contours and arrows are the concentration gradient distribution, concentration distribution under diffusive flux, and sum of the convective

and diffusive flux from top to bottom, respectively. The chaotic convection comprises an erratic concentration distribution, which happens mostly at high Re. Here, Re=60 is high enough to cause chaotic mixing

performance of proposed MURU in a wide range of Re and Pe to investigate the flow characteristic effects. The simulations were performed in four regions of Re: 0.001–0.1 (with a ratio of 10), 0.2–1 (with an increment of 0.1), 2–10 (with an increment of 1) and, 15–65 (with an increment of 5). The performance of the micromixer can be described by looking at the dominant mixing mechanisms in two regions depending on the critical Re ( $Re_c$ ): the diffusion-based mixing region ( $Re < Re_c$ ) and the convection-based mixing region ( $Re > Re_c$ ). In the diffusion-dominant region (Fig. 5b), the

mixing index is inversely proportional to Re, while in the convection-dominant region (Fig. 5c), this effect is contrariwise. For instance, in relatively small Re ( $Re \ll 0.1$ ), the fluids have become thoroughly mixed within a short length from the channel entrance. Therefore, for a given length, the mixing index increases after the critical velocity, where diffusion no longer plays a vital role in the mixing mechanism, and convection mixing occurs instead. As can be seen, the Re and mixing index vary proportionally within this region. Moreover, it can be concluded from Fig. 5 that contrary to

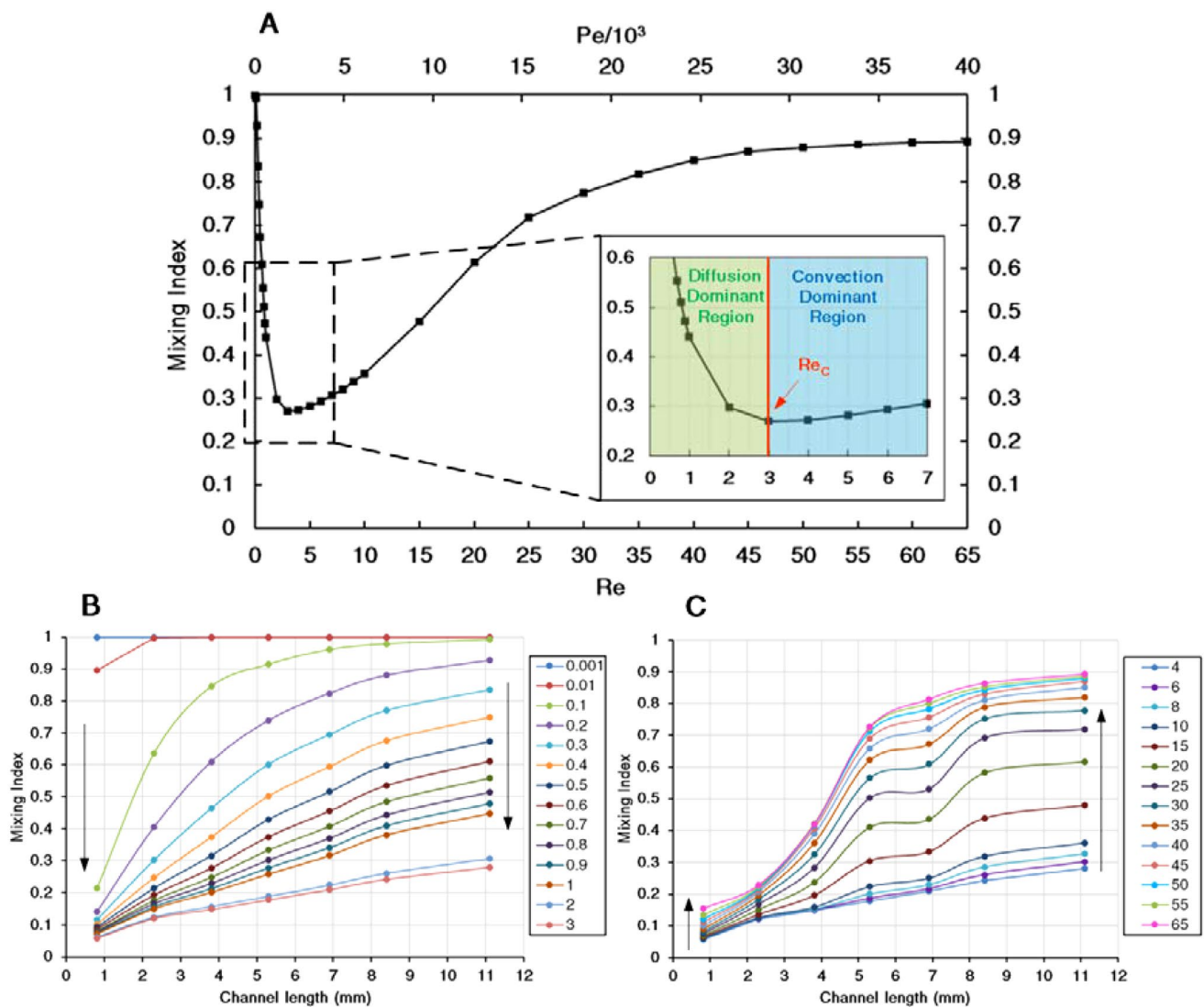


**Fig. 5** Analysis of the optimized micromixer. **a** The mixing performance of the optimized micromixer over a wide range of  $Re$  and  $Pe$  and the effect of  $Re$  on the local mixing index **b** before and **c** after the

critical  $Re$  ( $Re_c$ ). As arrows are indicating, before the critical  $Re$ , the mixing efficiency falls by the flow velocity increment, while after the critical point, the mixing efficiency would increase

the third unit, the fourth unit is the least effective unit in the entire channel. Figure 6 illustrates the velocity distribution and profiles at symmetrical axes accompanied by flow streamlines at different cross-sections, approximately before and after each unit. At the beginning of the bifurcate channel, where two flows enter the main channel, the velocity profile is expected to be in the form of that of in the Poiseuille flow. Approaching the first unit, the fluid starts to change its direction resulting in the relocation of peak velocity. The same condition happens in the next section; however, as a consequence of changing the direction of the mixing unit, the peak velocity happens near the opposing wall of the main channel. Moreover, a counter-rotating pair of vortices emerge owing to the flow swing, which likely

happens for every unit. Consequently, the diffusional path decreases while the mixing index increases. Note that G units induce quadruple vortices, which have a fluctuation in the widthwise velocity profile to favor the convection mixing. Thus, a vorticity analysis is provided for the third unit to understand its performance. Figure 7 shows the stream-wise vorticities in the third unit, G unit. The formula to calculate the vorticity vector,  $2\omega$ , is written as the curl of the flow velocity field (Eq. 13):

$$2\omega = \nabla \times 2V, \quad (13)$$

where  $\nabla$  is the del operator. As indicated, each branch contributes to the mixing of fluids with a similar flow rate. Indeed, a sense of symmetry is evident, although the unit

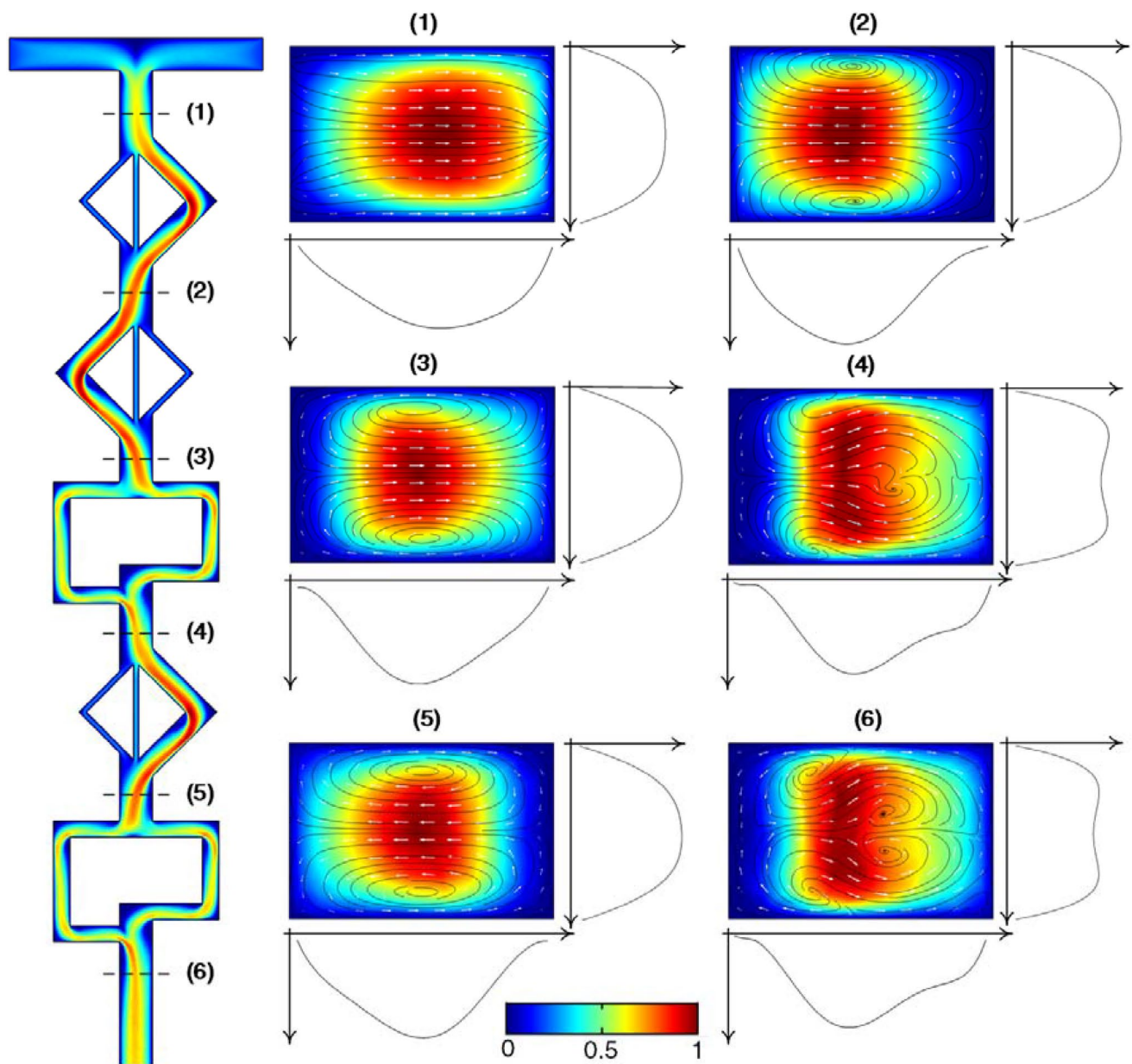


**Fig. 6** Illustration of the velocity distribution and fluctuation at different sections of the final design at  $Re=60$ . The graphs show the mid-plane velocity distributions (reported as non-dimensional values) next

to their axes. The sectional vortices and the variation of peak velocity location, as a factor of fluid mass, help the chaotic mixing to occur

is not symmetrical. This is true for the regions before the recombination point. A curvature-induced pair of vortices enters the unit and after encountering the opposing wall at the split point, a perpendicular pair of vortices forms and remains inside the channel until they reach the corners. As a consequence of the sharp curvature at the corners, the Dean flow starts to appear and persist through that region. Dean flow happens once again after the next corner through the branches by the time they merge to create quadruple vortices: a flow pattern caused by two chaotic flows recombining

perpendicularly. Therefore, it may be concluded that this unit is the most efficient part of the whole micromixer thorough the induction of chaotic flow. However, this can create a high-pressure drop inside the micromixer following the vortex pressure loss  $\sim U^n$  ( $n > 1$ ).

Figure 8a, b illustrate the pressure distribution at different  $Re$  along the dimensionless channel lengths of the nominated MURU of this study and the previously proposed MURO (Bazaz et al. 2018). The value of pressure at the channel in  $Re$  of 55 for MURO is  $\sim 84$  kPa, while for MURU is just  $\sim 6.3$  kPa.

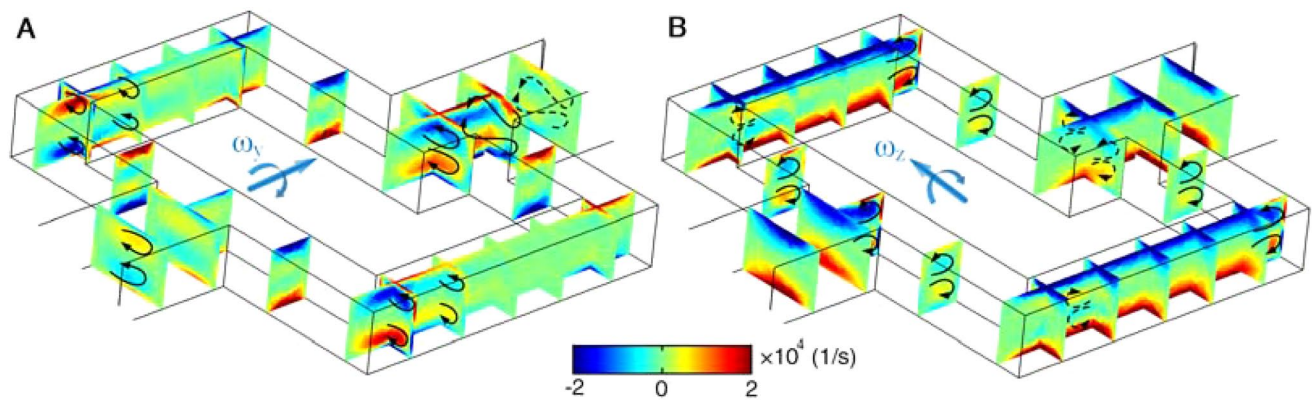


**Fig. 7** Stream-wise vorticities distribution ( $2\omega$ ) in the G unit located at the third slot drawn along the fluid pathways. Arrows showed in the dashed line demonstrate weak vorticities

It shows that the current strategy used in this study can reduce the input pressure 13 times, which is significant and facilitate the operating of devices. Below the Re of 75, MURU operates at input pressure lower than 10 kPa, and even at Re of 85, the input pressure is 12 kPa, which is significantly lower than micromixers in which obstacles are implanted. Looking into details reveal that the third and fifth units of MURU and the second, third, and fourth units of MURO are the most efficiently selected units in each case. As expected, the value of  $\frac{-\partial P}{\partial l}$  increases when reaching these types of units in either case. Moreover, the pressure drop is non-linearly correlated to the Re due to the inherent nonlinearity of flow within these units, where the effect of circulation in pressure loss is more significant compared with other units.

Finally, the two hybrid micromixers (MURU and MURO) are compared in Fig. 8c, d. The more the Re, the less the ratio of the pressure drop (% MURU/MURO pressure drop). At Re 1, the pressure drop ratio is around 10, while at Re of 55, it reaches 7.6. The comparison of the mixing index versus pressure drop for these two MURO and MURU is also depicted in Fig. 8d. MURO can proffer a higher mixing index at the cost of pressure drop while MURU gives an adequate level of mixing with a significantly lower pressure drop. Based on this diagram, a proper micromixer can be selected according to the user's demand. These results highlight the point that the simple design of present obstacle-free MURU can dramatically reduce the fabrication and operation cost, material, time, and energy for a broader range of mixing operations.

## 4 Conclusion

In this study, we evaluated the repetitive behavior of four distinctive mixing units, including convergent–divergent, circular, rhombic, and G-shaped micromixers to form an efficient hybrid planar micromixer with low-pressure drop. A well-known statistical method proposed by Taguchi was used to reduce the number of experiments from 1024 possible combinations of units to only 16 specific combinations. This method enabled us to thoroughly study the sensitivity of each unit and their order along the micromixer. The proposed efficient obstacle-free hybrid micromixer contains rhombic and G-shaped units to reach a high level of mixing index ( $> 80\%$ ) over a wide range of Re 0.001–0.3 and 35–65. The performance of the nominated design was investigated for Re ranging between 0.001 and 65 to examine its critical point (i.e., Re = 3) where the mechanism of mixing changes from diffusion to advection. Furthermore, a comprehensive investigation was carried out on the velocity fields, mixing index, concentration fields, and its gradients at different sections of the obstacle-free hybrid micromixer to examine its performance. The results led to the conclusion that the third unit, a G-shaped unit, has the most influence on the mixing performance containing chaotic advection through the quadruple vortices generated. Finally, a comparison between the present micromixer and previously proposed MURO micromixer proved the MURU has significantly

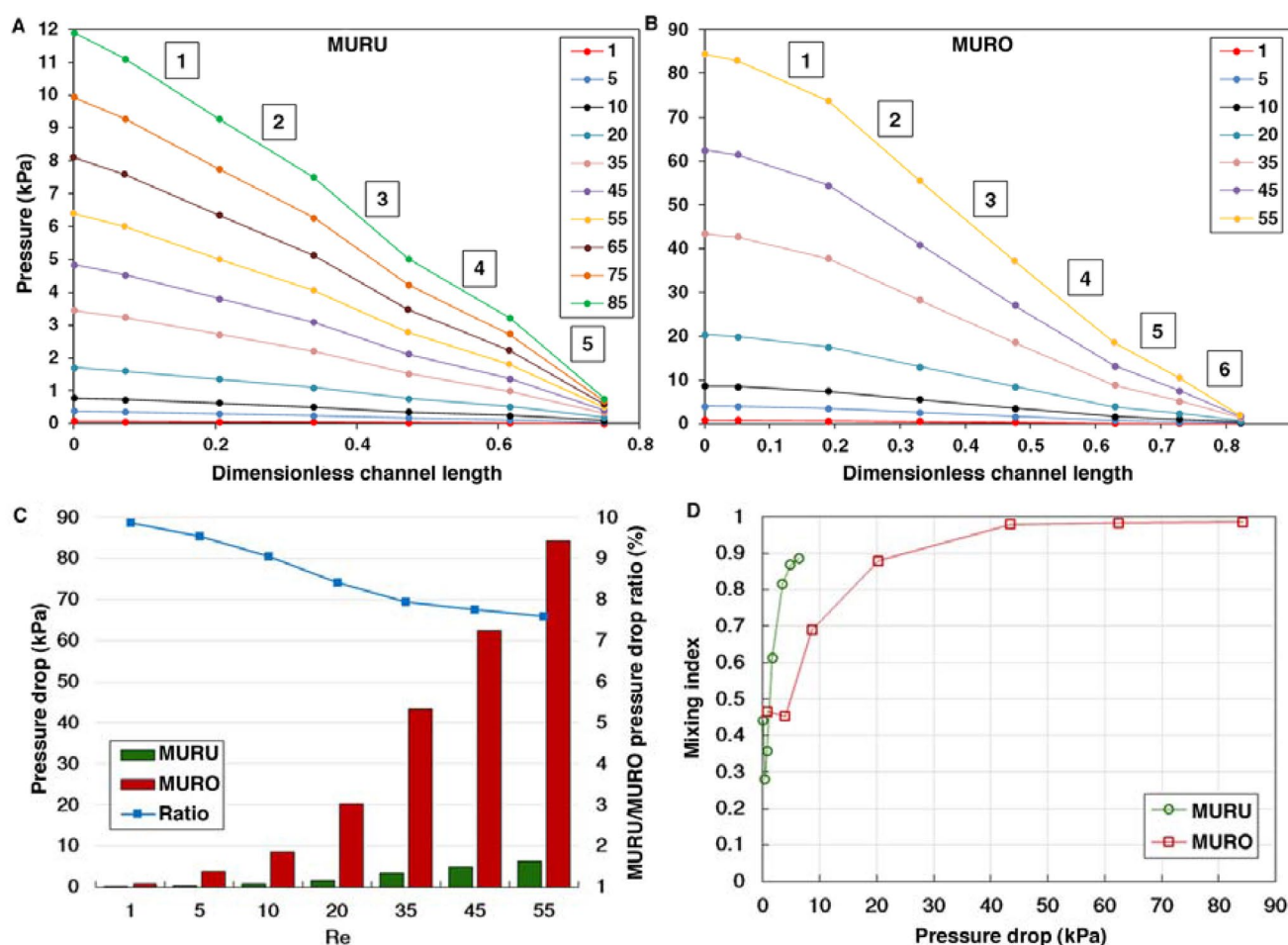


**Fig. 8** Pressure drop along the channels of **a** Taguchi-nominated MURU and **b** MURO micromixer at different Re, approximately before and after each unit. Locations of the slots are shown by their numbers over the graphs. It shows that the obstacle-free hybrid micromixer has a significantly lower pressure drop compared to

MURO. Analysis of pressure drop in micromixers; **c** the overall pressure drops of MURU and MURO designs at different Re and the ratio of them and **d** the variation of mixing index versus pressure drop (right). It is inferred that the power consumption can be reduced by at least 90% using MURU design at a constant Re

lower pressure drop while maintaining a relatively high mixing index. This further necessitates the development of planar micromixers with repetitive unites for the low-cost lab-on-a-chip and point-of-care devices. As a future goal, we highlight the investigation on integrated 3D units via the Taguchi method since it has worked for the previous 2D cases, and the pressure loss can be added as the response/objective function of the DOEM.

**Acknowledgements** M.E.W. would like to acknowledge the support of the Australian Research Council through Discovery Project Grants (DP170103704 and DP180103003) and the National Health and Medical Research Council through the Career Development Fellowship (APP1143377).

## References

- Afzal A, Kim K-Y (2012) Passive split and recombination micromixer with convergent–divergent walls. *Chem Eng J* 203:182–192
- Afzal A, Kim K-Y (2015) Convergent–divergent micromixer coupled with pulsatile flow. *Sens Actuators B Chem* 211:198–205. <https://doi.org/10.1016/j.snb.2015.01.062>
- Ansari MA, Kim K-Y, Anwar K, Kim SM (2010) A novel passive micromixer based on unbalanced splits and collisions of fluid streams. *J Micromech Microeng* 20(5):055007. <https://doi.org/10.1088/0960-1317/20/5/055007>
- Bahiraie M, Mazaheri N (2018a) Second law analysis for flow of a nanofluid containing graphene–platinum nanoparticles in a minichannel enhanced with chaotic twisted perturbations. *Chem Eng Res Des* 136:230–241. <https://doi.org/10.1016/j.cherd.2018.05.017>
- Bahiraie M, Mazaheri N (2018b) Application of a novel hybrid nanofluid containing graphene–platinum nanoparticles in a chaotic twisted geometry for utilization in miniature devices: thermal

- and energy efficiency considerations. *Int J Mech Sci* 138:337–349. <https://doi.org/10.1016/j.ijsmecsci.2018.02.030>
- Bahiraee M, Mazaheri N, Alighardashi M (2017) Development of chaotic advection in laminar flow of a non-Newtonian nanofluid: a novel application for efficient use of energy. *Appl Therm Eng* 124:1213–1223. <https://doi.org/10.1016/j.applthermaleng.2017.06.106>
- Bahiraee M, Mazaheri N, Bakhti A (2018) Irreversibility characteristics of nanofluid flow under chaotic advection in a minichannel for different nanoparticle types. *J Taiwan Inst Chem Eng* 88:25–36. <https://doi.org/10.1016/j.jtice.2018.04.002>
- Bayareh M, Ashani MN, Usefian A (2019) Active and passive micromixers: a comprehensive review. *Chem Eng Process Process Intensif*. <https://doi.org/10.1016/j.cep.2019.107771>
- Bazaz SR, Mehrizi AA, Ghorbani S, Vasilescu S, Asadnia M, Warkiani ME (2018) A hybrid micromixer with planar mixing units. *RSC Adv* 8(58):33103–33120. <https://doi.org/10.1039/c8ra05763j>
- Bhopte S, Sammakia B, Murray B Numerical study of a novel passive micromixer design. In: 2010 12th IEEE Intersociety conference on thermal and thermomechanical phenomena in electronic systems, 2–5 June 2010. pp 1–10. <https://doi.org/10.1109/ITHERM.2010.5501318>
- Boken J, Soni SK, Kumar D (2016) Microfluidic synthesis of nanoparticles and their biosensing applications. *Crit Rev Anal Chem* 46(6):538–561. <https://doi.org/10.1080/10408347.2016.1169912>
- Brouzes E, Medkova M, Savenelli N, Marran D, Twardowski M, Hutchison JB, Rothberg JM, Link DR, Perrimon N, Samuels ML (2009) Droplet microfluidic technology for single-cell high-throughput screening. *Proc Natl Acad Sci* 106(34):14195–14200
- Cai G, Xue L, Zhang H, Lin J (2017) A review on micromixers. *Micromachines* 8(9):274
- Chung C-K, Shih T (2007) A rhombic micromixer with asymmetrical flow for enhancing mixing. *J Micromech Microeng* 17(12):2495
- Condina MR, Dilmetz BA, Razavi Bazaz S, Meneses J, Ebrahimi Warkiani M, Hoffmann P (2019) Rapid separation and identification of beer spoilage bacteria by inertial microfluidics and MALDI-TOF mass spectrometry. *Lab Chip* 19(11):1961–1970. <https://doi.org/10.1039/C9LC00152B>
- Eun TH, Kim S-H, Jeong W-J, Jeon S-J, Kim S-H, Yang S-M (2009) Single-step fabrication of monodisperse TiO<sub>2</sub> hollow spheres with embedded nanoparticles in microfluidic devices. *Chem Mater* 21(2):201–203. <https://doi.org/10.1021/cm8017133>
- Fu L-M, Wang Y-N, Liu C-C (2014) An integrated microfluidic chip for formaldehyde analysis in Chinese herbs. *Chem Eng J* 244:422–428. <https://doi.org/10.1016/j.cej.2014.01.085>
- Gambhire S, Patel N, Gambhire G, Kale S (2016) A review on different micromixers and its micromixing within microchannel. *Int J Curr Eng Technol* 4:409–413
- Hessel V, Löwe H, Schönfeld F (2005) Micromixers—a review on passive and active mixing principles. *Chem Eng Sci* 60(8):2479–2501
- Hossain S, Kim K-Y (2014) Mixing analysis of passive micromixer with unbalanced three-split rhombic sub-channels. *Micromachines* 5(4):913–928
- Kwon T, Prentice H, De Oliveira J, Madziva N, Warkiani ME, Hamel J-FP, Han J (2017) Microfluidic cell retention device for perfusion of mammalian suspension culture. *Sci Rep* 7(1):6703
- Lashkaripour A, Silva R, Densmore D (2018a) Desktop micromilled microfluidics. *Microfluid Nanofluid* 22(3):31
- Lashkaripour A, Mehrizi AA, Goharimanesh M, Rasouli M, Bazaz SR (2018b) Size-controlled droplet generation in a microfluidic device for rare dna amplification by optimizing its effective parameters. *J Mech Med Biol* 18(01):1850002. <https://doi.org/10.1142/s0219519418500021>
- Lashkaripour A, Rodriguez C, Ortiz L, Densmore D (2019) Performance tuning of microfluidic flow-focusing droplet generators. *Lab Chip* 19(6):1041–1053. <https://doi.org/10.1039/C8LC01253A>
- Lee C-Y, Fu L-M (2018) Recent advances and applications of micromixers. *Sens Actuators B Chem* 259:677–702. <https://doi.org/10.1016/j.snb.2017.12.034>
- Lee C-Y, Wang W-T, Liu C-C, Fu L-M (2016) Passive mixers in microfluidic systems: a review. *Chem Eng J* 288:146–160
- Li J, Xia G, Li Y (2013) Numerical and experimental analyses of planar asymmetric split-and-recombine micromixer with dislocation sub-channels. *J Chem Technol Biotechnol* 88(9):1757–1765. <https://doi.org/10.1002/jctb.4044>
- Liu C, Guo J, Tian F, Yang N, Yan F, Ding Y, Wei J, Hu G, Nie G, Sun J (2017) Field-free isolation of exosomes from extracellular vesicles by microfluidic viscoelastic flows. *ACS Nano* 11(7):6968–6976
- Mahmoodi Z, Mohammadnejad J, Razavi Bazaz S, Abouei Mehrizi A, Ghiass MA, Saidijam M, Dinarvand R, Ebrahimi Warkiani M, Soleimani M (2019) A simple coating method of PDMS microchip with PTFE for synthesis of dexamethasone-encapsulated PLGA nanoparticles. *Drug Deliv Transl Res* 9(3):707–720. <https://doi.org/10.1007/s13346-019-00636-z>
- Mahmoudi Z, Mohammadnejad J, Razavi Bazaz S, Abouei Mehrizi A, Saidijam M, Dinarvand R, Ebrahimi Warkiani M, Soleimani M (2019) Promoted chondrogenesis of hMCSs with controlled release of TGF- $\beta$ 3 via microfluidics synthesized alginate nanogels. *Carbohydr Polym*. <https://doi.org/10.1016/j.carbpol.2019.115551>
- Mollajan M, Bazaz SR, Mehrizi AA (2018) A thoroughgoing design of a rapid-cycle microfluidic droplet-based PCR device to amplify rare DNA strands. *J Appl Fluid Mech* 11(1):21–29
- Nguyen N-T, Wu Z (2004) Micromixers—a review. *J Micromech Microeng* 15(2):R1
- Nilsson J, Evander M, Hammarström B, Laurell T (2009) Review of cell and particle trapping in microfluidic systems. *Anal Chim Acta* 649(2):141–157. <https://doi.org/10.1016/j.aca.2009.07.017>
- Raoufi MA, Razavi Bazaz S, Niazmand H, Rouhi O, Asadnia M, Razmjou A, Ebrahimi Warkiani M (2020) Fabrication of unconventional inertial microfluidic channels using wax 3D printing. *Soft Matter* 16(10):2448–2459. <https://doi.org/10.1039/C9SM02067E>
- Rasouli M, Abouei Mehrizi A, Goharimanesh M, Lashkaripour A, Razavi Bazaz S (2018) Multi-criteria optimization of curved and baffle-embedded micromixers for bio-applications. *Chem Eng Process Process Intensif* 132:175–186. <https://doi.org/10.1016/j.cep.2018.08.021>
- Razavi Bazaz S, Rouhi O, Raoufi MA, Ejeian F, Asadnia M, Jin D, Ebrahimi Warkiani M (2020a) 3D printing of inertial microfluidic devices. *Sci Rep* 10(1):5929. <https://doi.org/10.1038/s41598-020-62569-9>
- Razavi Bazaz S, Mashhadian A, Ehsani A, Saha SC, Krüger T, Ebrahimi Warkiani M (2020b) Computational inertial microfluidics: a review. *Lab Chip* 20(6):1023–1048. <https://doi.org/10.1039/C9LC01022J>
- Tavassoli H, Alhosseini SN, Tay A, Chan PP, Oh SKW, Warkiani ME (2018) Large-scale production of stem cells utilizing microcarriers: a biomaterials engineering perspective from academic research to commercialized products. *Biomaterials* 181:333
- Uson L, Sebastian V, Arruebo M, Santamaria J (2016) Continuous microfluidic synthesis and functionalization of gold nanorods. *Chem Eng J* 285:286–292. <https://doi.org/10.1016/j.cej.2015.09.103>
- Vasilescu SA, Bazaz SR, Jin D, Shimoni O, Warkiani ME (2020) 3D printing enables the rapid prototyping of modular microfluidic devices for particle conjugation. *Appl Mater Today*. <https://doi.org/10.1016/j.apmt.2020.100726>
- Wang Y-N, Yang R-J, Ju W-J, Wu M-C, Fu L-M (2012) Convenient quantification of methanol concentration detection utilizing an

- integrated microfluidic chip. *Biomicrofluidics* 6(3):034111. <https://doi.org/10.1063/1.4746246>
- Whitesides GM (2006) The origins and the future of microfluidics. *Nature* 442(7101):368–373
- Yi C, Li C-W, Ji S, Yang M (2006) Microfluidics technology for manipulation and analysis of biological cells. *Anal Chim Acta* 560(1):1–23
- Zhang T, Hong Z-Y, Tang S-Y, Li W, Inglis DW, Hosokawa Y, Yalikun Y, Li M (2020) Focusing of sub-micrometer particles in microfluidic devices. *Lab Chip*. <https://doi.org/10.1039/C9LC00785G>

**Publisher's Note** Springer Nature remains neutral with regard to jurisdictional claims in published maps and institutional affiliations.